



# Micro-Structure Analysis of Quasi-Static Crushing and Low-Velocity Impact Behavior of Graded Composite Metallic Foam Filled Tube

Youssef Taraz Jamshidi<sup>1</sup> · Ali Pourkamali Anaraki<sup>1</sup> · Mojtaba Sadighi<sup>2</sup> · Javad Kadkhodapour<sup>1</sup> · Seyed Mohammad Hossein Mirbagheri<sup>3</sup> · Behnaz Akhavan<sup>4</sup>

Received: 30 August 2019 / Accepted: 10 October 2019 / Published online: 4 December 2019  
© The Korean Institute of Metals and Materials 2019

## Abstract

Foam filled tubes (FFT) are novel structures with high energy absorption, enhanced strength to weight ratio, and tailoring capability. In the present paper, we have analyzed quasi-static uniaxial compression and low-velocity impact behavior of FFT with closed-cell metallic foam cores and functionally graded densities both experimentally and numerically. Alporas foams were manufactured using liquid state method with TiH<sub>2</sub> blowing agent. We prepared Specimens with graded composition and densities by stacking of several layers of pure aluminum and A356 alloy Alporas foams with cubic geometry. We conducted several standard uniaxial compression experiments to determine the non-linear mechanical properties and hardening. Square aluminum tubes are manipulated to enhance the performance and tailoring specification of the structure. We generated microstructural models using a hybrid 3D Voronoi diagram and CT-scan images to predict mechanical behavior numerically. Computed tomography is used to determine the inner cells morphological characterization. Also, the modified Kelvin cell with a beam element in edge regions is manipulated to enhance accuracy. Comparing the quasi-static experiment and FEA results show good accordance, and hence, we achieved the calibrated model. Finally, we used the numerical model in FFT tailoring and mechanical properties design.

**Keywords** Microstructure · Foam filled tube (FFT) · Voronoi diagram · FEM · Graded cellular solid

## 1 Introduction

Cellular solids, especially metal foams, have rather irregular microstructure [1]. So generating a micro-model is essential for mechanical behavior analysis. There are several methods for geometrical modeling of cellular structures such as Kelvin and other unit cells, Voronoi diagrams, CT scan images

geometric reconstruction, stochastic placement of voids, and soap froth. Furthermore, there are several standard methods for material properties characterization, such as uniaxial compression and tension, microhardness, and Nanoindentation. Microstructural damage investigation with SEM and optical microscopes has done by Yuan. They model microstructure using Kelvin unit cell with thin shell faces and simulate uniaxial compression and effect of cell edges material properties by FEM and experiments [2]. Kadkhodapour et al. present an approach bridging micro-deformation to macro-mechanical properties in closed-cell metallic foams using FEM and experiments. They used several unit cells such as spherical and elliptical, to model micro-structure and investigated the effects of relative density and topology [3]. A comprehensive study is conducted on Alporas foam mechanical properties by Jang et al. they analyzed foam specimen shape and dimensions and their effects on uniaxial compression behavior. They employed various unit cells in the numerical modeling of cellular structure [4]. Nammi et al. are also worked on closed-cell lattice numerical modeling using unit cell approach. They used spherical-cubic and cruciform cells

✉ Ali Pourkamali Anaraki  
ali\_pourkamali@sru.ac.ir

<sup>1</sup> Department of Mechanical Engineering, Shahid Rajaei Teacher Training University, Lavizan, Tehran 1678815811, Iran

<sup>2</sup> Department of Mechanical Engineering, Amirkabir University of Technology, Hafez St., Tehran 1591634311, Iran

<sup>3</sup> Department of Mining and Metallurgical Engineering, Amirkabir University of Technology, Hafez, Tehran 1591634311, Iran

<sup>4</sup> Department of Industrial Engineering, Islamic Azad University, Tehran North Branch, Tehran 1651153311, Iran

in modeling as well as tetrakaidecahedron Kelvin cell. They compared numerical results with experiments [5].

Song et al. used 3D irregular Voronoi and regular tetrakaidecahedron model for finite element modeling of closed-cell foams. They studied irregularity, relative density, and hardening effects, and also dynamic impact loading on mechanical behavior. They showed that a proper increase in irregularity might increase energy absorption capacity [6]. Sotomayor et al. proposed a method for modeling 6101-T6 open-cell aluminum alloy based on a 3D Voronoi approach. They studied the effects of irregularity and foam density in elastic–plastic compression based on semi-empirical and analytical methods and mainly focused on density variation [7]. Zheng et al. incorporated a 3D finite element method for uniaxial dynamic impact simulation on metallic foams using 2D and 3D Voronoi model. Their investigations focused on the plastic deformation mechanism and shear failure in microstructures [8]. Zhang et al. conducted an FEA investigation on the mesoscopic model of closed-cell foams using a 3D Voronoi approach. They manipulated the Voronoi nucleus, and shell face thickness to control cell size and porosity. Also, plastic deformation and cell wall cracking in the mesoscale closed-cell lattice due to large compression and tension are analyzed [9]. 3D Voronoi tessellation is manipulated by Li et al. to model the mesoscale model for closed-cell foams for finite element analysis. Also, they simulated loading on cellular solids using homogeneous models. The study focused on impact velocity, irregularity, relative density, micro-inertia, and crushing stress [10]. Graded foam manufacturing is quite complicated. He et al. manufactured density graded Alporas using the special cooling procedure. Quasi-static and dynamic impact loading is analyzed using these graded specimens [11].

Sun et al. investigated density graded FFT and its effects on the crashworthiness and energy absorption characteristics. Their method is FEA simulations and particle swarm optimization (SPO). The main objective functions are energy absorption and crushing peak force [12]. Li et al. studied experimentally the mechanical behavior and energy absorption capability of circular tubes filled with aluminum foam. They also studied empty tubes and double-layered FFT specimens. The loading condition is oblique and static. Tubes are made from AA6063-T6 alloy, and aluminum foam has approximately 450 kg per cubic meter density [13]. Axial crushing behavior of ex situ aluminum FFT specimens is studied experimentally. Duarte et al. produced aluminum foam using powder metallurgy method. Their main research objectives are failure mode and energy absorption determination [14]. Crashworthiness of CFRP and metallic circular tubes filled with various foams are investigated experimentally under axial loading conditions. The core materials are aluminum honeycomb and metallic foams [15]. Altin et al. studied experimentally the effect of fill ratio for foam-filled

tubes with circular and rectangular cross-sections as well as single and multi-cell tubes under axial crushing conditions. They manipulated explicit dynamic approach and finite element analysis for verification purposes [16]. High temperature crushing behavior of circular tubes filled with A356 aluminum foam is studied experimentally. Movahedi et al. analyzed the energy absorption capacity of FFT structures at 300 °C [17]. Quasi-static lateral crushing of foam-filled circular tubes is studied both analytically and experimentally by Liu et al. [18].

Baroutaji et al. conducted comprehensive studies for recent applications and future development of foam-filled tubes [19]. Sun et al. studied energy absorption and crushing force of various single and multi-cell FFT structures. They also present optimization strategies for efficient FFT topological configuration determination based on multi-objective decision making named COPRAS [20]. Crushing characteristics determination of in situ FFT produced using powder metallurgy with very thin thickness are conducted experimentally. Duarte et al. used quasi-static axial loading and infrared thermography [21]. Experimental and analytical investigation of square cross-section FFT filled with density graded aluminum foam is performed by Yu et al. [22]. Sun et al. studied crushable foam plasticity and mesoscopic geometrical models. They studied mechanical behavior, and energy absorption capability of CFRP and metallic tubes filled with aluminum foams both numerically and experimentally [23]. Comparative crashworthiness analysis for thin-walled FFT and empty tubes is conducted. Li et al. investigated the effect of tube cross-section and foam fill ratio on energy absorption [24]. Zhang et al. studied the dynamic impact and crushing of double-layered FFT specimens filled with aluminum foams both numerically and experimentally. They manipulated computed tomography (CT) technique for geometry reconstruction and finite element method for numerical simulation. Also they investigate mesoscopic deformation and energy absorption of FFT under high-velocity impact condition [25]. Yi et al. conducted the energy absorption enhancement of aluminum FFT using FEA and tailoring the structure characteristics by placing various aluminum foam layers. Foams are in graded form with respect to radial coordinate in density parameter [26]. Quasi-static crushing and dynamic impact response of hybrid FFT with open-cell metallic foams and epoxy resin are investigated using infrared thermography [27]. Rajak et al. analyzed axial compression behavior of AlSi10 Mg aluminum foam-filled tubes experimentally. Aluminum foam is produced using melting method and its density varies from 450 to 850 kg per cubic meter. Experiments are conducted with 0.1–10 per second strain rate. In each rate energy absorptions are compared. They used analysis of variance (ANOVA) to determine the significant factors in energy absorption [28].

In the present paper, we analyzed quasi-static and low-velocity impact behavior of FFT with graded density and mechanical properties experimentally and numerically. Firstly, the numerical model calibration is conducted using material characterization, CT-scan images, and FEM. Microstructural model of the cellular core is generated using a Voronoi diagram. Finally, the calibrated model is manipulated to determine the macroscopic specifications of FFT and tailoring structures in static and dynamic loading conditions. So using the hybrid FEA and microstructural numerical model yields to mechanical properties and energy absorption characteristics design. Finally, we obtained the microstructural model and its morphological specifications for desired macro-mechanical properties such as energy absorption density.

## 2 Materials and Methods

### 2.1 Experimental Methods

#### 2.1.1 Specimen Preparation

To produce closed cell Aluminum foam, liquid state method with 2 percent TiH<sub>2</sub> and 1.5 percent Calcium is manipulated. Additives are used as blowing agent and viscosity enhancer respectively, at 680 °C. Manufactured blocks have 100 × 50 × 10 cm dimensions. For FFT production, cubic foams of 21.5 mm dimensions with various densities and chemical compositions are cut using a band saw. Precision sizing of specimens is performed by CNC milling and EDM wire cut. Finally, 16 pure and 22 A356 aluminum alloy foams are manufactured with different densities. Cutting from a different height of foam block yields a variety of densities for grading purpose. For graded FFT production, foam cubes are stacked in square tubes with two and three layers. In Table 1, specimens composition, dimensions, and densities are included.

Foam density distribution is generally 300–400 and 400–500 kg/m<sup>3</sup> for pure aluminum and A356 alloy, respectively. Aluminum alloy 1100 tube used in FFT has a square profile, 24 × 24 outer dimensions and 1 mm thickness. Various FFT configurations with two and three-layer stacking and densities are manufactured as in Table 2. Furthermore, several auxiliary tests are performed for characterization purposes such as tubes with various heights and simple foam specimens in uniaxial crushing loading.

#### 2.1.2 Quasi-static Uniaxial and Characterization Experiments

Standard uniaxial tension test is conducted to determine the mechanical properties of an aluminum tube made of 1100

alloy, according to ASTM B557 (2014). Also, standard tests are performed on pure and A356 composition foams according to ISO 13314 (2011) for characterization purpose. Comparing experimental results with the literature [29] shows good agreements. Mechanical behavior analysis of FFT is performed using quasi-static compression testing of various graded structures using ZWICK 100 apparatus with 5 mm/min loading rate [30]. In Fig. 1, quasi-static uniaxial compression test setup and crushing mode of FFT is shown.

## 2.2 Numerical Methods

### 2.2.1 Problem Description

For the mechanical behavior determination of specific structures, the most important step is the finite element model generation. Micro-structural modeling of FFT is achieved using a 3D Voronoi diagram with controlled lattice irregularity. Furthermore, classic tetrakaidecahedron Kelvin cells are modified using 3D beam elements to model scaffold structures and cell edges. Numerical investigations are focused basically on quasi-static uniaxial compression, and low-velocity impact behavior prediction of density and chemical composition graded FFT with different layers. Analysis outputs are generally macroscopic variables such as Young's modulus, plateau stress, peak stress, densification strain, and energy absorption capacity. Calibrating FE models using appropriate experiments yields to tailoring FFT structures and designing corresponding mechanical properties in static and dynamic loading conditions. Furthermore, non-graded single-layer specimens are also analyzed. Generating Voronoi lattice is based on choosing  $N$  points in 3D space, each representing cells nuclei. Nucleus placement with controlled disturbance distribution yields to desired micro-structural model. To model regular tetrakaidecahedron cellular solid, cell nuclei should be placed with a distance  $d_0$  as below [6], [10] and [29].

$$d_0 = \frac{\sqrt{6}}{2} \left( \frac{V_0}{\sqrt{2}N} \right)^{\frac{1}{3}} \quad (1)$$

Also, the degree of irregularity parameter  $k$  is defined to model controlled irregular lattice as  $k = 1 - \delta/d_0$ . In which  $\delta$  is the minimum distance between two consecutive nuclei. So  $\delta = d_0$  yields to  $k = 0$  and the regular lattice is achieved. In Fig. 2, micro-structural model with 20% irregularity is shown.

### 2.2.2 FEA Implementation and Assumptions

Using hybrid Voronoi micro-structural model and FE method yields to a micro model which accurately describe

**Table 1** Manufactured aluminum foam cubic specimens

No.	Mat.	mass (mg)	l (mm)	w (mm)	h (mm)	Density (kg/m <sup>3</sup> )
1	Al.	3.56	21.5	21.5	20.5	376
2		3.87	21.5	21.5	21	399
3		3.55	21.5	21.5	20.5	375
4		3.55	21.5	21.5	21.5	357
5		3	21.5	21.5	20.5	317
6		3.62	21.5	21.5	21.5	364
7		3.17	21.5	21.5	21.5	319
8		2.87	21.5	21.5	20	310
9		3.08	21.5	21.5	20.5	325
10		3.07	21.5	21.5	20.5	324
11		4.02	21.5	21.5	21	414
12		3.08	21.5	21.5	21.5	310
13		3	21.5	21	20	332
14		3.17	21.5	21.5	21	327
15		3.79	21.5	21.5	21	390
16	A356	2.76	21.5	21.5	20	299
1		4.32	21.5	21.2	21.2	447
2		4.51	21.5	21	21	476
3		4.14	21.5	21.5	21	426
4		4.97	21.5	21	21	524
5		5	21.5	21	21	527
6		4.42	21.5	21.5	20.5	466
7		5.46	21.5	21.2	21	570
8		5.52	21.5	21	21	582
9		4.95	21.5	21.5	21	510
10		4.52	21.5	21	21	477
11		4.84	21.5	21	21	510
12		3.97	21.5	21.5	21	409
13		4.91	21.5	21.5	21	506
14		5.12	21	21	21.5	540
15		4.64	21.5	21.2	21.2	480
16	4.63	21	21.5	21	488	
17	3.67	21	21	21	396	
18	5.82	21	21.2	21.5	608	
19	6.99	21.5	21.2	21.2	723	
20	4.57	21.5	21	21.2	477	
21	4.52	21.5	21.5	21.2	461	
22	4.68	21.5	21.5	21.5	471	

mechanical behavior. The calibrated numerical model is obtained using several simulations with various irregularity distribution perturbed around an average value. The average value of irregularity is determined by processing high-resolution digital images and CT scan. The irregularity value is chosen to be 10%–20% to obtain the best fit of the micro model and cell distribution. Cell faces are modeled using conventional linear shell elements with reduced integration and quadrilateral geometry or simply S4R. To model cell edges, 3D linear beam element, B31 is used. Explicit dynamics procedure is manipulated

in ABAQUS 2017 to simulate FFT mechanical behavior. Also, 3D quadrilateral rigid elements R3D4 are used to model compression plateaus of loading device and drop weight hammer impactor [31].

General contact formulation with hard normal is used to model surface interactions. Also, tangential behavior is assumed to have a friction coefficient of 0.1 [29]. Perturbing the mean value of the friction coefficient do not affect outputs significantly. Bi-linear hardening model is used to employ aluminum plastic deformation. Material properties are shown in Table 3. Density graded foams are obtained

**Table 2** Quasi-static uniaxial compression experiments

Test no.	Layers	Mat/specimen configuration	Layer densities *
R1	2	A15 → A17	317 → 319
R2	2	AS4 → AS5	524 → 527
R3	2	AS2 → A18	476 → 310
R4	2	A19 → AS9	325 → 510
R5	3	A110 → AS10 → AS11	324 → 477 → 510
R6	3	AS13 → A112 → AS14	506 → 310 → 540
R7	3	AS15 → AS16 → A113	480 → 488 → 332
R8	3	A114 → AS20 → A116	327 → 477 → 299
R9	3	AS21 → AS22 → AS6	461 → 471 → 466
R10	–	Tube 01–66 mm	–
R13	–	Tube 02–44 mm	–
B1	1	A1	322
B2	1	AS	435

\*Foam densities arranged from bottom to top (kg/cubic m)

using different cell size, face thickness, and edge profile dimensions [32]. In quasi-static compression simulations, loading is modeled by the constant velocity of the movable rigid plateau and fixing another plateau. The loading rate is increased as much as output error is negligible to enhance computational efficiency. Also, smooth step loading with continuous slope is used to reduce output noise. Anti-aliasing real-time and Butterworth filters with 2 kHz cutoff frequency are used to noise elimination [33]. Due to the high elongation of pure aluminum and A356 alloy, ductile damage initiation criterion is used with zero energy value for damage evolution depend on stress triaxiality  $\eta = -p/q$ . In which  $p$  and  $q$  are von-Mises equivalent stress and hydrostatic stress respectively [34, 35].

Outputs are reported as nominal stress and strains using a nominal cross-sectional area and a total height of specimens. Generally, for low-velocity impact analysis, outputs are given in impact force time history., Firstly, linear Eigen-buckling analyses are conducted, and tube buckling mode shapes are extracted to enhance the simulation accuracy. These shapes

**Fig. 1** Quasi-static test setup and FFT deformation mode, **a** universal test apparatus, **b** undeformed FFT, **c–h** deformed FFT with 10 to 60 percent strain



**Fig. 2** **a** Micro-structure model of foam specimen with 20% irregularity, **b** typical Kelvin cell with 20% irregularity, **c** cell parameters definitions

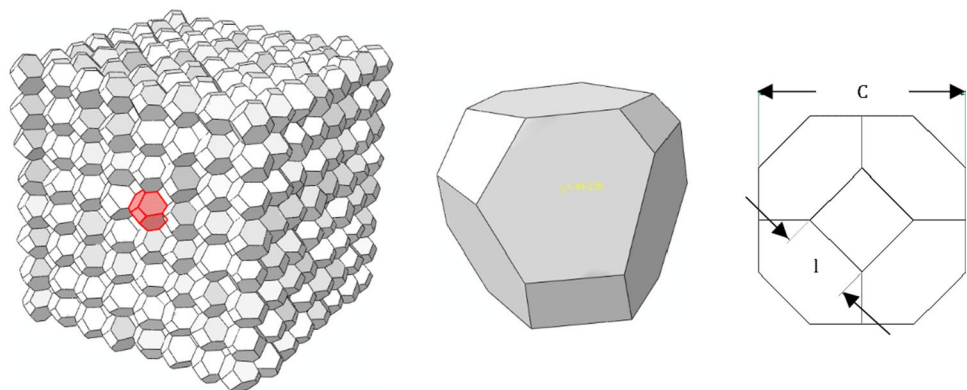


**Table 3** Material mechanical and physical properties

Material	$\rho$ (kg/m <sup>3</sup> )	$E$ (GPa)	Tangent modulus (GPa)	$\sigma_y$ (MPa)	$\nu$
Al [29]	2700	69	0.47	76	0.35
A356 [36]	2670	69	0.0	130	0.35
1100 alloy [37]	2710	70	0.2	122	0.34

are manipulated for geometric imperfection implementation on tubes to simulate its crushing more precise.

### 2.2.3 Low-Velocity Impact Simulation

In low-velocity impact simulations, according to the drop hammer experiments, impactor mass is 14 kg. Also, due low friction in sliders, which is proven by a high-speed camera, impact velocity is about 3.7 m/s corresponding to 70 cm release height. In other words, impact energy is about 96 J [38].

### 2.2.4 Densification Strain and Plateau Stress

Two major parameters affecting energy absorption capacity and mechanical behavior of metallic foams are densification strain  $\varepsilon_d$  and plateau stress  $\sigma_{pl}$ . Densification strain is approximately  $1 - 1.4\rho^*/\rho_s$ . In which  $\rho^*$  and  $\rho_s$  are cellular structure and solid material densities respectively. To determine the above parameters, a more precise method based on energy absorption could be used [39, 40].

$$E(\sigma_a) = \frac{\int_{\varepsilon_{cr}}^{\varepsilon_a} \sigma(\varepsilon) d\varepsilon}{\sigma(\varepsilon_a)} \quad (2)$$

In which energy absorption efficiency  $E(\sigma_a)$  is defined as the amount of energy absorbed from initial yielding strain  $\varepsilon_{cr}$  to corresponding strain  $\varepsilon_a$  normalized to corresponding stress  $\sigma_a = \sigma(\varepsilon_a)$ . Initial yielding point is defined as the first peak in the stress–strain curve. Densification strain could be determined by maximizing energy absorption efficiency, or

$$\frac{dE(\varepsilon)}{d\varepsilon} = 0 \Rightarrow \varepsilon = \varepsilon_d \quad (3)$$

Furthermore, plateau stress under compression loading is determined as below.

$$\sigma_{pl} = \frac{\int_{\varepsilon_{cr}}^{\varepsilon_d} \sigma(\varepsilon) d\varepsilon}{\varepsilon_d - \varepsilon_{cr}} \quad (4)$$

## 2.2.5 Microstructure Morphological Parameters Determination

Cellular solid morphological parameters determination is essential for accurate microstructural modeling and consequent mechanical behavior prediction. These parameters are average values of cell size  $C$ , edge length  $l$ , face thickness  $t_f$ , edge profile dimension  $t_e$  and volume fraction of solid material in edges  $\varphi$ . In Fig. 2, the unit cell of microstructure with controlled irregularity and some major morphological parameters definition is shown.

Because of foam relative density  $\rho^*/\rho_s$  is the most effective factor in mechanical behavior, the main question is what are realistic morphological parameters corresponding to a relative density of each specimen [1]. The process of finding these values is iterative. Initial values are obtained using digital images and CT scan. Furthermore, average cell size has lower importance. Measuring  $\rho^*/\rho_s$  of specimens is quite simple. Observations show that the average cell size of pure aluminum and A356 is 4–5 mm. it is assumed that cubic foams in 21.5 mm tube inner dimensions considering 0.5 mm gap have five complete cells. Hence, the average cell size is 4.3 mm. For sensitivity analysis, four and six complete cells with 5.38 and 3.58 mm size are also analyzed, and negligible output variations achieved. Edge length also depends on cell size or  $l = C/(\sqrt{2})$ . For 5 cells edge length is 1.56 mm.

Another important parameter in precise micro-structural modeling is volume fraction  $\varphi$ . It relates  $t_f$  to  $t_e$  or  $\phi = t_e^2/(t_e^2 + Z_f t_f l/\bar{n})$ . In closed cell metallic foam, e.g. Alporas, it is about 0.6–0.8 [41]. In which  $Z_f$  and  $\bar{n}$  are a number of faces common in each edge and the average number of edges forming each face respectively. In most foams  $Z_f = 3$  and here  $\bar{n} = 5.14$ . To determine morphological parameters, desired foam density will be constrained as below.

$$\rho_{Al} \left\{ \frac{t_e^2 L_{edge} + t_f A_{total}^{finite}}{V_{total}} \right\} = \rho^* \quad (5)$$

In which  $\rho_{Al}$  is aluminum density,  $L_{edge}$  is a total length of edges in cellular solids,  $A_{total}^{finite}$  is the total face area in finite cells lattice and  $V_{total}$  is total structure volume. As mentioned, it is assumed that each cellular specimen with  $21.5 \times 21.5 \times 21.5$  mm dimensions and five complete cells in each row has 189 cells. So  $L_{edge}$ ,  $A_{total}^{finite}$  and  $V_{total}$  are 5017, 7600 and 7511 in a millimetric system of units. Finally, a variation of  $t_e$  and  $t_f$  could be obtained in terms of  $\phi$ . Processing CT and high-resolution images, as shown in Fig. 3 yields to initial range of  $\phi$  to be 0.65–0.75 [42]. Volume fraction is calculated using the average  $t_e/t_f$  ratio, determined from various CT images. The ratio is about

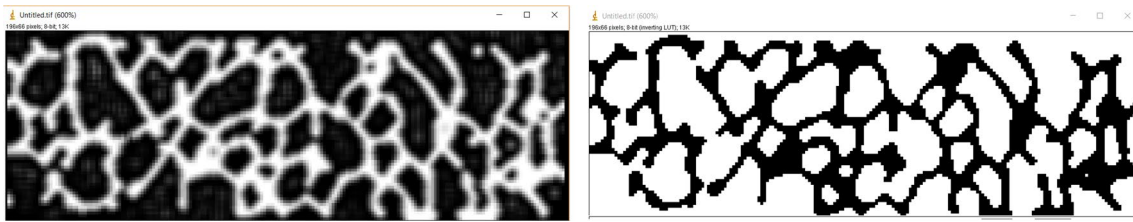


**Fig. 3** CT scan images **a** before and **b** after image processing for morphological parameters prediction

**Table 4** Morphological parameters of different foam densities

$\rho^*$ (kg/m <sup>3</sup> )	$\phi$	$t_e$ (mm)	$t_f$ (mm)	$t_f$ (mm)	$t_e/t_f$
300	0.6	0.279	0.058	0.058	4.8
	0.7	0.308	0.047	0.047	6.5
	0.8	0.341	0.034	0.034	10
400	0.6	0.322	0.078	0.078	4.1
	0.7	0.357	0.062	0.062	5.8
	0.8	0.394	0.044	0.044	9
500	0.6	0.361	0.097	0.097	3.7
	0.7	0.4	0.079	0.079	5.1
	0.8	0.441	0.055	0.055	8

5.0–6.0. The iterative process of FEA with different  $\phi$  values yields to calibrated FE model with minimum error. The optimum value of  $\phi$  is 0.7. Variation of  $\phi$ ,  $t_e$ ,  $t_f$  and  $t_e/t_f$  for different foam densities are tabulated in Table 4.

## 3 Results and Discussion

### 3.1 Numerical Model Verification

Several quasi-static uniaxial compression experiments are conducted for verification and calibration numerical model and also material properties characterization. These experiments are categorized into three groups as bare foam specimen, tubes with different heights, and graded FFT with two and three layers. Bare foams experiments are conducted using 322 kg/cubic meter pure aluminum and 435 kg/cubic meter A356 foam specimens with 40 mm dimensions. These experiments are named B1 and B2, respectively. All the tests are continued until full densification and sudden rise in stress. Comparison between experiment and FEA for B1 specimen is shown in Fig. 4. As depicted, good accordance in an average value of plateau stress and densification strain is obtained. Noisy experimental results for bare foams is related to the size effects and localized cell crushing. Generally, experiments are repeated three times for each specimen to ensure results reliability. Average experimental values of plateau stress and densification strain 1.6 MPa and 70%. These results

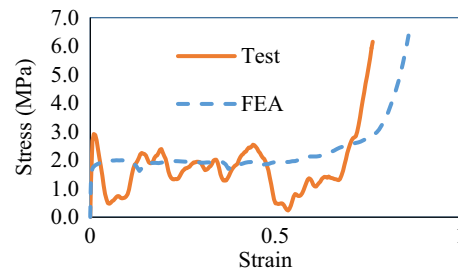


**Fig. 4** FEA and experimental results comparison for B1 test of Al bare foam (322 kg/cubic meter)

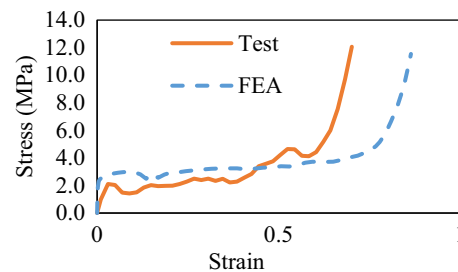


**Fig. 5** FEA and experimental results comparison for B2 test of A356 bare foam (435 kg/cubic meter)

are 1.9 MPa and 75% for FE simulation. Hence, there are 18% and 7% over-prediction error in numerical simulation.

In Fig. 5 experimental and numerical results comparison for A356 alloy is shown. Plateau stress and densification strain for A356 bare foam are 2.6 MPa and 63% for experiment and 3.1 MPa and 71% for FEA. There are 19% and 13% over-prediction error. So good agreement with maximum 20% error is achieved. Furthermore, comparing test and FEA for empty tubes are also showed very good accordance.

In Figs. 6 and 7 comparison between deformation modes for bare foam and tubes are shown respectively. Due to the importance of mesh independency analysis in FEM simulations, a comprehensive study is conducted with various mesh densities. For instance, uniaxial compression simulation is performed using approximately 37,000, 29,000, and 21,000 elements, which about 30%

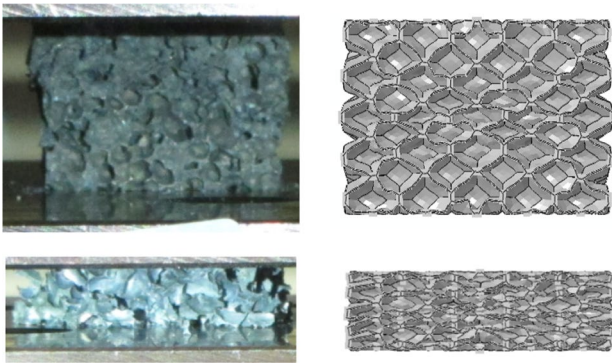


**Fig. 6** Experiment and FEA comparison of deformation mode of bare foam specimen, **a** and **b** un-deformed and deformed foam specimen in compression test, **c** and **d** un-deformed and deformed foam specimen in FEA

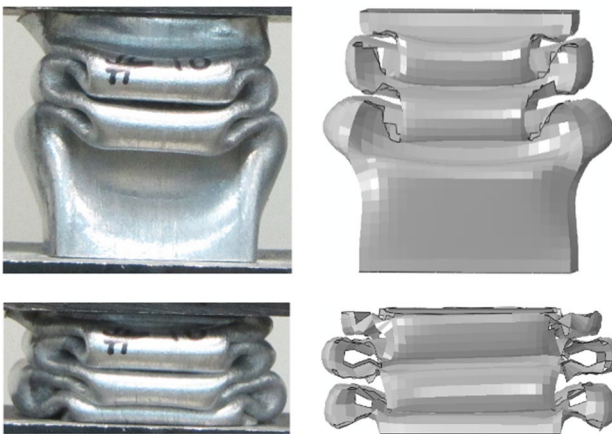


**Fig. 7** Experiment and FEA comparison of deformation mode of empty tube, **a** and **b** un-deformed and deformed tube specimen in compression test, **c** and **d** un-deformed and deformed tube specimen in FEA

was beam element, and the rest was shell element. Finally, the fine mesh with 1 mm global approximate element size is chosen due to the high computational cost and accuracy. Relative error corresponding to fine, medium, and coarse mesh is 20%, 33%, and 57% respectively. Using finer mesh increases computational cost while error decreases slightly. In Table 5 summary for experimental and numerical results comparison of the verification process is tabulated.

Furthermore, in Figs. 8 and 9 stress–strain curves corresponding to two and three layers graded FFT with Al325 → AS510, and Al324 → AS477 → AS510 configuration is shown respectively. The designation includes material composition and layers densities from bottom to top. In which Al is pure aluminum and AS is A356 alloy foam. As shown, there is good agreement between simulation and experiments, especially up to 50% strain. A considerable

error is observed in the densification region because of the nature of the shell model and contact formulation [10]. Fortunately, over-prediction in densification strain is almost constant, and it is predictable in other experiments. So the calibrated numerical model is obtained and could be manipulated in various static and dynamic simulations. Another point is that the maximum error is according to specific energy absorption density because of the multiplication of errors in  $\sigma_{pl}$  and  $\epsilon_d$ .

### 3.2 Quasi-Static Uniaxial Compression

In this section, various configurations of FFT and graded bare foams simulation results are presented, and correlations are proposed. To be more realistic, Al and AS layer densities are chosen to be 300 and 500 kg/cubic meter in simulations. Furthermore, the main focus is on the local behavior of graded structures. In other words, results are presented in detail for different phases on the stress–strain curve corresponding to graded structures. So designing mechanical properties and structural tailoring is achieved. In Tables 6, 7, 8 and 9 simulation results for various structures are presented such as three and two layers FFT and bare graded foam and also single layer FFT and bare foam.

Major output parameters are total ultimate nominal densification strain of the structure  $\epsilon_d^{ult}$ , energy absorption until ultimate densification  $E_{total}$  and total energy absorption density  $u_{total}$ , number of extremum points in energy absorption efficiency curve which are corresponding to different phases of plateau region and energy absorption due to density gradient  $N_{extr}^{Eff}$ , different local densification strain in each phase in ascending order  $\epsilon_d^{phases}$ , energy absorption density in each phase  $u_{phases}$  and finally plateau stress of distinct phases in the stress–strain curve  $\sigma_{pl}^{phases}$ . Analyzing the stress–strain curve of each specimen gives detailed comprehension. For instance, the number of extremum points on energy absorption efficiency curve is related to different densification regimes of structures. A most important parameter in mechanical behavior design and tailoring process is total energy absorption or crashworthiness. So a comprehensive bar chart is shown in Fig. 10. The result is used for crashworthiness decision making for desired energy absorption capacity as input and structural configuration as output.

According to the results, manipulating 28 various structures yielded to 15–435 J energy absorption. Furthermore, in a range of 90–130 J, there are several FFT and bare graded foam options. It is worth noting that bare and FFT specimens have 15–128 and 93–435 J energy absorption, respectively. The statistical study shows that structure configuration selection corresponding to desired energy absorption could be achieved within a maximum 20% variation. Also, to predict



**Table 5** Verification tests and simulation results summary

Test no.	Test 1			Test 2			Test 3			Test 4		
	FEA $\sigma_{max}$ (MPa) <sup>1</sup>	Test Error (%) <sup>2</sup>	FEA $\sigma_{pl}$ (MPa) <sup>3</sup>	Test Error (%) <sup>2</sup>	FEA $\epsilon_d$ (%) <sup>4</sup>	Test Error (%) <sup>2</sup>	FEA $u_{total}$ (MPa) <sup>5</sup>	Test Error (%) <sup>2</sup>				
R1	15	18.1	21	9.7	11.3	17	59	63	7	5.7	7.1	25
R2	14.7	18.1	23	14.8	13.0	-12	50	60	20	7.4	7.8	5
R3	15.1	18.1	20	10.7	12.4	15	57	68	19	6.1	8.4	38
R4	15.7	18.1	15	11.9	12.0	1	58	65	12	6.9	7.8	13
R5	13.8	18.2	32	11.4	12.3	8	49	73	49	5.6	9	61
R6	15.2	18.2	20	11.6	13.1	13	50	70	40	5.8	9.2	59
R7	14.2	18.2	28	11.3	13.6	20	52	77	48	5.9	10.5	78
R8	14.7	18.2	24	10.9	13.4	23	54	79	46	5.9	10.6	80
R9	14.6	18.2	25	12.9	13.8	6	51	72	41	6.6	9.9	50
R10	8	8.8	10	3.1	4.3	39	41	42	2	126	179	42
R13	7.8	10.5	35	3.5	4.5	28	31	35	13	109	158	45

<sup>1</sup>In tube tests, maximum force is reported in kN

<sup>2</sup>The relative error of simulation for test; + over-prediction and - under-prediction

<sup>3</sup>In tube tests, plateau force is reported in kN

<sup>4</sup>In tube tests, densification displacement is reported in mm

<sup>5</sup>In tube tests, the absorbed energy is reported in J

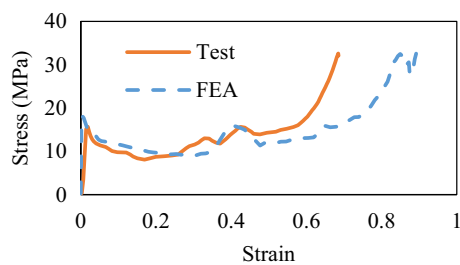


**Fig. 8** FEA and experimental results comparison for R4 test with Al325 → AS510 configuration

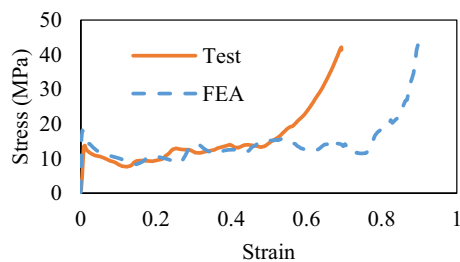


**Fig. 9** FEA and experimental results comparison for R5 test with Al324 → AS477 → AS510 configuration

mechanical properties, correlations are presented for the average density of structures.

In Fig. 11, energy absorption density is depicted for bare and FFT structures. As shown, linear regression for

variation is acceptable. So, increasing average density yields to increase in specific energy for both FFT and bare structure. In Fig. 12, linearly ascending trend for total plateau stress in bare and FFT structures is shown. In Figs. 13 and 14 variation of total densification strain for bare and FFT structures are shown respectively. As seen, there is a quadratic trend with a maximum point at about 370–400 kg/cubic meter.

### 3.3 Low-Velocity Impact

Verification of explicit dynamics procedure in quasi-static simulation and accelerated loading rates ensures the validity of the numerical model to predict low-velocity impact behavior. Because FFT structures are more applicable and their performance indices in energy absorption are superior, the present analysis focused on this kind of structures. Outputs are summarized as impact force time history and nominal stress–strain curves. Furthermore, results from interpretation yields to maximum force  $F_{max}$  and stress  $\sigma_{max}$ , average force  $F_{ave}$  and stress  $\sigma_{ave}$  in the semi-plateau region during impact, crushing displacement  $\delta_{cru}$  and strain  $\epsilon_{cru}$ , total specific energy  $u_{total}$  and energy absorption  $E_{total}$  and finally, impact time duration  $t_{imp}$ .

In Figs. 15 and 16 stress–strain and force time history for three layers FFT with Al → Al → Al (300)-T configuration is shown respectively. In Table 10, the whole simulation summary for various FFT in low-velocity impact is included. Four major performance indices are presented for tailoring purpose as maximum and average stress, crushing strain, and impact time duration. Also, in Figs. 17, 18, 19 and 20,

**Table 6** Quasi-static simulation results summary for 3 layers graded FFT

Structure	Configuration	$\epsilon_d^{ult}$ (%)	$u_{total}$ (MPa)	$E_{total}$ (J)	$N_{extr}^{Eff}$	$u_{phases}$ (MPa)	$\sigma_{pl}^{phases}$ (MPa)
3 layers graded FFT	Al → Al → Al-T	73	8.62	257	1	8.62	11.8
	Al → Al → AS-T	82	11.43	341	3	4.97, 2.15, 4.31	11.3, 14.3, 18.7
	Al → AS → Al-T	77	9.9	295	3	4.7, 2.1, 3.1	10.4, 15, 17.2
	Al → AS → AS-T	74	10.9	325	1	10.9	14.7
	AS → Al → Al-T	84	11.8	351	2	5.7, 6.1	11.6, 17.4
	AS → Al → AS-T	80	11.7	349	3	5.1, 4.2, 2.4	12.4, 16.8, 17.1
	AS → AS → Al-T	82	12.4	370	1	12.4	15.1
	AS → AS → AS-T	83	14.6	435	4	4.3, 2, 4.9, 3.4	14.8, 16.7, 18.8, 21.3

**Table 7** Quasi-static simulation results summary for 3 layers graded bare foam

Structure	Configuration	$\epsilon_d^{ult}$ (%)	$u_{total}$ (MPa)	$E_{total}$ (J)	$N_{extr}^{Eff}$	$\epsilon_d^{phases}$ (%)	$u_{phases}$ (MPa)	$\sigma_{pl}^{phases}$ (MPa)
3 layers graded bare foam	Al → Al → Al	77	1.7	49	3	55, 64, 77	1.1, 0.2, 0.36	2.0, 2.2, 2.8
	Al → Al → AS	78	2.5	75	2	48, 78	1.0, 1.5	2.1, 5.0
	Al → AS → Al	83	2.9	86	3	50, 76, 83	1.0, 1.4, 0.5	2.0, 5.4, 7.1
	Al → AS → AS	74	3.3	98	2	24, 74	0.5, 2.8	2.1, 5.6
	AS → Al → Al	78	2.5	73	2	48, 78	1.0, 1.5	2.0, 5.0
	AS → Al → AS	73	3.7	110	2	25, 73	0.5, 3.2	2.0, 6.7
	AS → AS → Al	73	3.2	95	2	22, 73	0.4, 2.8	1.8, 5.5
	AS → AS → AS	75	4.3	128	2	59, 75	3.1, 1.2	5.3, 7.5

**Table 8** Quasi-static simulation results summary for single and double layers FFT and bare foam

Structure	Configuration	$\epsilon_d^{ult}$ (%)	$u_{total}$ (MPa)	$E_{total}$ (J)	$N_{extr}^{Eff}$	$\epsilon_d^{phases}$ (%)	$u_{phases}$ (MPa)	$\sigma_{pl}^{phases}$ (MPa)
2 layers graded FFT	Al → Al-T	73	8.9	177	1	73	8.9	12.2
	Al → AS-T	77	11.2	223	3	50, 66, 77	6.1, 2.9, 2.2	12.2, 18.1, 20
	AS → Al-T	79	11.5	229	3	56, 74, 79	7.3, 3.2, 1.0	13.0, 17.8, 20
	AS → AS-T	73	12.7	252	2	58, 73	9.6, 3.1	16.6, 20.7
2 layers graded bare foam	Al → Al	69	1.5	29	2	59, 69	1.2, 0.3	2.0, 2.5
	Al → AS	80	3.3	66	2	35, 80	0.7, 2.6	2.0, 5.8
	AS → Al	80	3.25	65	2	37, 80	0.75, 2.5	2.0, 5.8
	AS → AS	70	4.1	81	1	70	4.1	5.9
Single layer FFT	Al-T	79	9.4	93	2	59, 79	5.7, 3.6	9.8, 17.3
	AS-T	73	12.3	122	1	73	12.3	16.8
Single layer bare foam	Al	64 to 73	1.3 to 1.5	12.9 to 14.9	1	64 to 73	1.3 to 1.5	About 2.0
	AS	70	4.2	42	1	70	4.2	6.0

**Table 9** Quasi-static simulation results summary for various square hollow tubes

Structure	Height (mm)	Thickness (mm)	$\epsilon_d^{ult}$ (%)	$u_{total}$ (MPa)	$E_{total}$ (J)	$\sigma_{pl}$ (MPa)
Square hollow tube	22	1.0–1.1	74	5.3	56	7.2
	44		68	5.6	119	8.2
	66		73	5.6	179	7.6

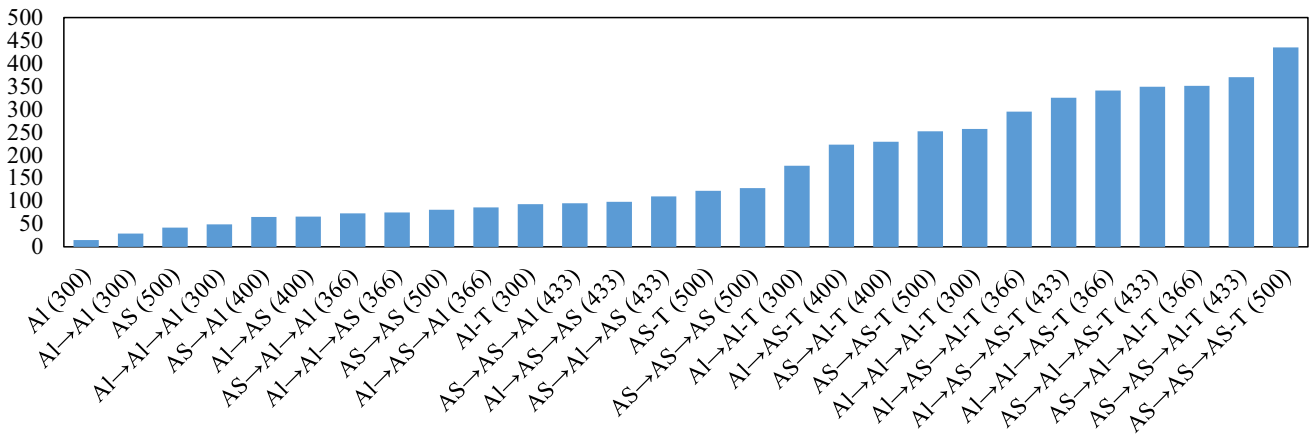


Fig. 10 Crashworthiness and tailoring chart for energy absorption capacity

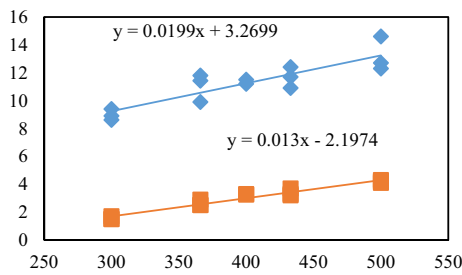


Fig. 11 Total energy absorption density for bare (bottom) and FFT (top) structures with linear correlation

correlations are presented for these parameters. Non-linear variations are obviously seen for impact loading condition.

### 4 Conclusions

The present research focused on designing mechanical properties and crashworthiness of FFT and bare foam structures based on experimentally calibrated microstructural finite element model both for quasi-static and low-velocity impact loading conditions. Also, we tried to

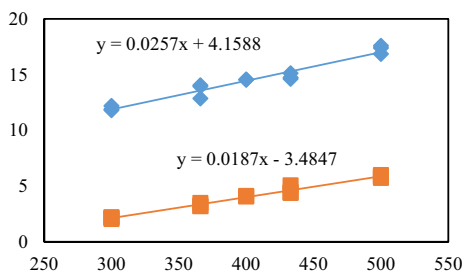


Fig. 12 Total plateau stress for bare (bottom) and FFT (top) structures with linear correlation

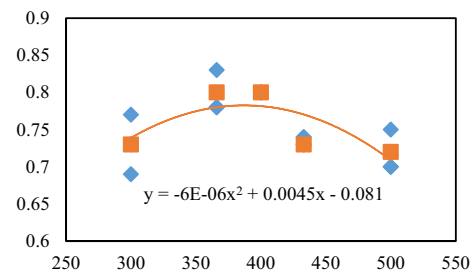


Fig. 13 Densification strain for bare structures with quadratic correlation – average (filled square) and raw data (filled diamond)

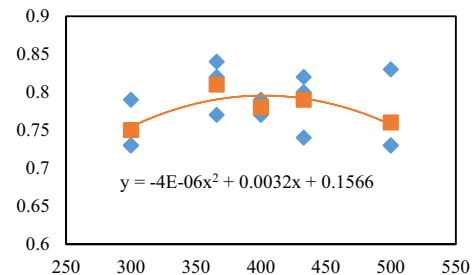


Fig. 14 Densification strain for FFT structures with quadratic correlation – average (filled square) and raw data (filled diamond)

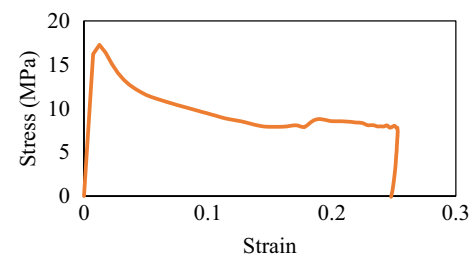
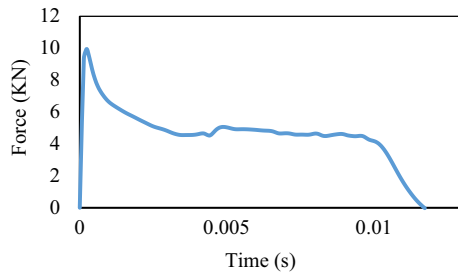


Fig. 15 Stress-strain curve in low velocity impact for Al->Al->Al(300)-T configuration



**Fig. 16** Force time history in low velocity impact for Al→Al→Al (300)-T configuration

bridge between microscale to macroscale properties using micro numerical model. In other words, using desired macro-mechanical properties such as energy absorption or several densification regions, the microstructural model and its morphological parameters could be determined precisely. So the main achievements are summarized below.

- Micro-structural geometric and FE model is generated based on a modified Kelvin cell with beam elements on the edges and 3D Voronoi diagram with controlled irregularity.
- The digital image processing technique is manipulated on CT scan and high-resolution stereo images to initialize the morphological parameters such as  $\varphi$  and  $t_e/t_f$  for error minimization in model generation.
- Numerical model is calibrated using quasi-static experimental results and model limitations are determined e.g. densification strain and region prediction.
- Several correlations are presented to predict  $\sigma_{pl}$ ,  $\epsilon_d$  and  $u_{total}$  of bare and FFT structures in static loading concerning average density.
- Macro and micromechanical properties and crashworthiness index could be tailored in static and dynamic loading conditions.
- The wide variety of graded structures in the form of bare foam and FFT with 15–435 J and maximum 20% variation increment in energy absorption capacity is obtained.
- Energy absorption density and plateau stress have linearly ascending behavior for quasi-static loading of bare and FFT in terms of average density.
- Densification strain variation in terms of average density is convex upward with a quadratic form for bare and FFT in static loading. The maximum densification strain occurs at 370–400 kg/cubic meter densities.
- Accurate dynamic behavior prediction is achieved using a calibrated numerical model and correlations for  $\sigma_{max}$ ,  $\sigma_{ave}$ ,  $\epsilon_{crn}$  and  $t_{imp}$  are proposed.
- In low-velocity impact, maximum stress is reached just after impact, and its trend is ascending with density.

**Table 10** Low velocity impact simulation results summary for 2 and 3 layers FFT

Structure	Configuration	$\sigma_{max}$ (MPa)	$F_{max}$ (kN)	$\sigma_{ave}$ (MPa)	$F_{ave}$ (kN)	$\epsilon_{crn}$ (%)	$\delta_{crn}$ (mm)	$u_{total}$ (MPa)	$E_{total}$ (J)	$t_{imp}$ (ms)
Graded 3 layers FFT	Al→Al→Al-T	17.3	10.0	9.7	5.6	25.3	16.7	2.45	93.1	11.7
	Al→Al→AS-T	17.5	10.1	9.2	5.3	27.0	17.8	2.47	93.9	12.1
	Al→AS→Al-T	17.4	10.0	9.1	5.2	27.1	17.9	2.46	93.5	12
	Al→AS→AS-T	17.6	10.1	11.3	6.5	21.5	14.2	2.43	92.4	9.4
	AS→Al→Al-T	16.8	9.7	9.5	5.4	25.6	16.9	2.42	92.0	11.7
	AS→Al→AS-T	17	9.8	9.1	5.2	26.2	17.3	2.38	90.5	11.6
	AS→AS→Al-T	17.4	10.0	9.9	5.7	24.7	16.3	2.45	93.1	10.7
	AS→AS→AS-T	17.6	10.1	12.5	7.2	19.7	13	2.47	93.9	8.5
Graded 2 layers FFT	Al→Al-T	16.4	9.4	10.2	5.9	36.4	16	3.7	93.8	10.9
	Al→AS-T	16.6		10.0	5.8	37.0	16.3	3.7	93.8	10.3
	AS→Al-T	16.6		9.7	5.6	37.0	16.3	3.6	91.2	10.2
	AS→AS-T	17.2		12.2	7.0	30.0	13.2	3.65	92.5	8.6

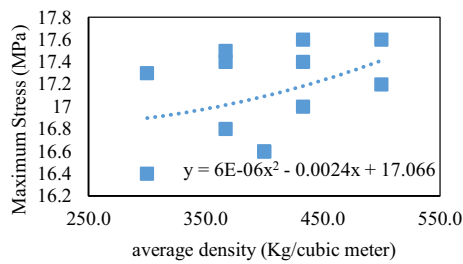


**Fig. 17** Maximum impact stress variation for FFT structures with upward concave parabolic correlation

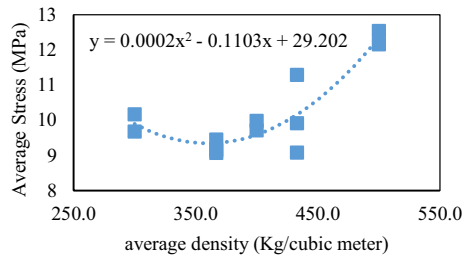


**Fig. 18** Average impact stress variation for FFT structures with upward concave parabolic correlation

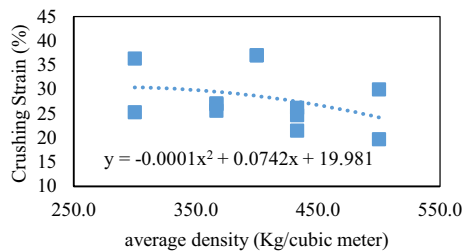


**Fig. 19** Crushing strain variation for FFT structures with downward concave parabolic correlation

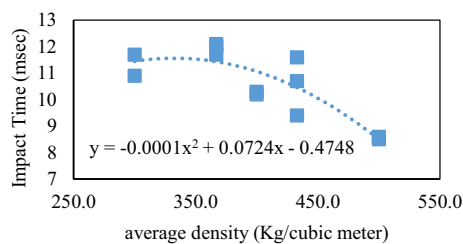


**Fig. 20** Impact time variation for FFT structures with downward concave parabolic correlation

The same result is seen for  $\sigma_{ave}$  except in low average densities.

- Ultimate crushing strain and impact time are descending in low-velocity impact for average density. But the decreasing rate of  $t_{imp}$  is more than  $\epsilon_{cru}$ .

## References

1. M. Ashby, A. Evans, N. Fleck, L.J. Gibson, *Metal Foams: A Design Guide* (Butterworth-Heinemann Publications, Oxford, 2000)
2. J-y Yuan, Y-x Li, Effects of cell wall property on compressive performance of aluminum foams. *Trans. Nonferrous Met. Soc. China* **25**, 1619–1625 (2015)
3. J. Kadkhodapour, S. Raeisi, Micro–macro investigation of deformation and failure in closed-cell aluminum foams. *Comput. Mater. Sci.* **83**, 137–148 (2014)
4. W.-Y. Jang, W.-Y. Hsieh, C.-C. Miao, Y.-C. Yen, Microstructure and mechanical properties of ALPORAS closed-cell aluminium foam. *Mater. Charact.* **107**, 228–238 (2015)
5. S. Nammi, P. Myler, G. Edwards, Finite element analysis of closed-cell aluminium foam under quasi-static loading. *Mater. Des.* **31**, 712–722 (2010)
6. Y. Song, Z. Wang, L. Zhao, J. Luo, Dynamic crushing behavior of 3D closed-cell foams based on Voronoi random model. *Mater. Des.* **31**, 4281–4289 (2010)
7. O.E. Sotomayor, H.V. Tippur, Role of cell regularity and relative density on elastoplastic compression response of 3-D open-cell foam core sandwich structure generated using Voronoi diagrams. *Acta Materialia* **78**, 301–313 (2014)
8. Z. Zheng, H. Wang, J. Yu, S.R. Reid, J.J. Harrigan, Dynamic stress-strain states for metal foams using a 3D cellular model. *J. Mech. Phys. Solids* (2014)
9. C. Zhang, L. Tang, B. Yang, L. Zhang, X. Huang, D. Fang, Meso-mechanical study of collapse and fracture behaviors of closed-cell metallic foams. *Comput. Mater. Sci.* **79**, 45–51 (2013)
10. Z. Li, J. Zhang, J. Fan, Z. Wang, L. Zhao, On crushing response of the three-dimensional closed-cell foam based on Voronoi model. *Mech. Mater.* **68**, 85–94 (2014)
11. S.-Y. He, Y. Zhang, G. Dai, J.-Q. Jiang, Preparation of density-graded aluminum foam. *Mater. Sci. Eng. A* **618**, 496–499 (2014)
12. G. Sun, G. Li, S. Hou, S. Zhou, W. Li, Q. Li, Crashworthiness design for functionally graded foam-filled thin-walled structures. *Mater. Sci. Eng. A* **527**, 1911–1919 (2010)
13. Z. Li, J. Yu, L. Guo, Deformation and energy absorption of aluminum foam-filled tubes subjected to oblique loading. *Int. J. Mech. Sci.* **54**, 48–56 (2012)
14. I. Duarte, L. Krstulovic-Opara, M. Vesjenjak, Characterisation of aluminium alloy tubes filled with aluminium alloy integral-skin foam under axial compressive loads. *Compos. Struct.* **121**, 154–162 (2015)
15. G. Sun, S. Li, Q. Liu, G. Li, Experimental study on crashworthiness of empty/aluminum foam/honeycomb filled CFRP tubes. *Compos. Struct.* **15**, 969 (2016)
16. M. Altin, M.A. Güler, S.K. Mert, The effect of percent foam fill ratio on the energy absorption capacity of axially compressed thin-walled multi-cell square and circular tubes. *Int. J. Mech. Sci.* **131–132**, 368–379 (2017)
17. N. Movahedi, E. Linul, Quasi-static compressive behavior of the ex-situ aluminum-alloy foam-filled tubes under elevated temperature conditions. *Mater. Lett.* **206**, 182 (2017)
18. Z. Hung, Q. Qin, Z. Liu, Experimental and theoretical investigations on lateral crushing of aluminum foam-filled circular tubes. *Compos. Struct.* **175**, 19 (2017)
19. A. Baroutaji, M. Sajjiaab, A.-G. Olabic, On the crashworthiness performance of thin-walled energy absorbers: recent advances and future developments. *Thin-Wall. Struct.* **118**, 137–163 (2017)
20. G. Sun, T. Liu, X. Huang, G. Zhen, Q. Li, Topological configuration analysis and design for foam filled multi-cell tubes. *Eng. Struct.* **155**, 235–250 (2018)

21. I. Duarte, L. Krstulović-Opara, M. Vesenjak, Axial crush behaviour of the aluminium alloy in situ foam filled tubes with very low wall thickness. *Compos. Struct.* **192**, 184–192 (2018)
22. Q. Qin, J. Zhang, S. He, C. Xiang, M. Wang, T. Wang, X. Yu, Crushing and energy absorption of density-graded foam-filled square columns: experimental and theoretical investigations. *Compos. Struct.* **201**, 423 (2018)
23. Z. Wang, H. Yu, Z. Gong, Q. Li, G. Sun, Experimental and numerical investigation into the crashworthiness of metal foam-composite hybrid structures. *Composite Structures* **209**, 535 (2018)
24. Z. Li, R. Chen, F. Lu, Comparative analysis of crashworthiness of empty and foam-filled thin-walled tubes. *Thin-Wall. Struct.* **124**, 343–349 (2018)
25. L. Chen, H. Wu, Q. Fang, Y. Zhang, J. Zhang, Experimental and mesoscopic investigation of double-layer aluminum foam under impact loading. *Compos. Struct.* (2019)
26. Z. Yi, H.S.-Y.L. Jia-gui, Z. Wei, G. Xiao-lu, Y. Jin, Density gradient tailoring of aluminum foam-filled tube. *Compos. Struct.* **220**, 451–459 (2019)
27. I. Duarte, L. Krstulović-Opara, J. Dias-de-Oliveira, M. Vesenjak, Axial crush performance of polymer-aluminium alloy hybrid foam filled tubes. *Thin-Wall. Struct.* **138**, 124–136 (2019)
28. D.K. Rajak, N.N. Mahajan, E. Linul, Crashworthiness performance and microstructural characteristics of foam-filled thin-walled tubes under diverse strain rate. *J. Alloys Compd.* **775**, 675–689 (2019)
29. L. Li, P. Xue, Y. Chen, H. Butt, Insight into cell size effects on quasi-static and dynamic compressive properties of 3D foams. *Mater. Sci. Eng. A* **636**, 60–69 (2015)
30. W. Yan, E. Durif, Y. Yamada, C. Wen, Crushing simulation of foam-filled aluminium tubes. *Mater. Trans. Jpn. Inst. Met.* **48**(7), 1901–1906 (2007)
31. J. Němeček, V. Králík, J. Vondřejc, A two-scale micromechanical model for aluminium foam based on results from nanoindentation. *Comput. Struct.* **128**, 136–145 (2013)
32. Z. Li, Z. Zheng, J. Yu, J. Yang, F. Lu, Spherical indentation of closed-cell aluminum foams: An empirical force–depth relation. *Mater. Sci. Eng. A* **618**, 433–437 (2014)
33. Y. Taraz Jamshidi, *Comprehensive Guide to Mechanical Analysis with ABAQUS*, 4th Ed, Afrang Pub., Orange Triangle Series, Tehran (2017)
34. ABAQUS Documentation, Dassault Systemes Simulia Corp., 2017
35. Y. TarazJamshidi, M. Salehi, *Engineering Elasticity, Applications and Problems*, 2nd edn. (Amirkabir University Press, Tehran, 2017)
36. R. Nunes, J. Adams, M. Ammons, *ASM Handbook, Vol 2, Properties and Selection: Non-ferrous Alloys and Special Purpose Materials* (ASM International, Cleveland, 1992)
37. I. Ghobadi, *Tensile Test Report, Contract No. 8413* (Razi Lab, Tehran, 2018)
38. M. Sadighi, M.M. Aghdam, S.M.H. Mirbagheri, S. Talebi, Micro–macro analysis of closed-cell aluminum foam with crushing behavior subjected to dynamic loadings. *Mater. Today Commun.* **13**, 170 (2017)
39. S.K. Maiti, L.J. Gibson, M.F. Ashby, Deformation and Energy Absorption Diagrams for Cellular Solids. *Acta Metallurgica* **32**, 1963–1975 (1984)
40. V.S. Deshpande, N.A. Fleck, Isotropic constitutive model for metallic foams. *J. Mech. Phys. Solids* **48**, 1253–1276 (2000)
41. L.J. Gibson, M.F. Ashby, *Cellular Solids, Structures and Properties*, 2nd edn. (Cambridge Publication, Cambridge, 1997)
42. M. Sadighi, M.M. Aghdam, S. Talebi, The effect of impact energy parameters on the closed-cell aluminum foam crushing behavior using X-ray tomography method. *AUT J. Mech. Eng.* **2**, 105–114 (2018)

**Publisher's Note** Springer Nature remains neutral with regard to jurisdictional claims in published maps and institutional affiliations.